Journal of Materials Chemistry A

Radiofrequency-Triggered Surface-Heated Laser-Induced Graphene Membranes for Enhanced Membrane Distillation

Journal:	*Journal of Materials Chemistry A*
Manuscript ID	TA-ART-08-2024-005611.R1
Article Type:	Paper
Date Submitted by the Author:	25-Oct-2024
Complete List of Authors:	Mahbub, Md Hasib Al; Texas Tech University, Chemical Engineering Nowrin, Fouzia Hasan; Texas Tech University, Chemical Engieering; Texas Tech University Saed, Mohammad; Texas Tech University, Department of Electrical & Computer Engineering Malmali, Mahdi; Texas Tech University, Department of Chemical Engineering

Radiofrequency-Triggered Surface-Heated Laser-Induced Graphene Membranes for Enhanced Membrane Distillation

*Hasib Mahbub,[1] Fouzia Hasan Nowrin,[1] Mohammad A. Saed,[2] Mahdi Malmali[1]**

[1]Department of Chemical Engineering, Texas Tech University, Lubbock, Texas 79409, United States

[2] Department of Electrical & Computer Engineering, Texas Tech University, Lubbock, Texas 79409, United States

**Corresponding author email address: mahdi.malmali@ttu.edu; Tel.: (806) 834-8706; Fax: (806) 742-3552*

Abstract

Membrane distillation (MD) has attracted significant research interest for desalinating hypersaline brine. However, the lack of robust hydrophobic membrane and lower energy efficiency requirements restrict its true potential. Designing and fabricating a hydrophobic membrane that enables surface heating at the mass transfer interface provides a potential route for efficient desalination with MD. This study aims to study a new class of surface-heated membranes that can be triggered by radiofrequency (RF) electromagnetic waves. We developed hydrophobic membranes that were prepared by CO_2 laser ablation of polyethersulfone (PES) membrane substrate. Proposed single-step laser modification converts PES membrane surface to laser-induced graphene (LIG), which is hydrophobic and electroconductive, making it suitable for surface heating. The hydrophobic nature of the prepared PES-LIG membrane is confirmed from surface water contact angle (147.3°), and surface heating potential is studied by investigating the thermal response of the membrane exposed to RF fields. Membrane surface average temperature can reach up to ~140 °C with optimized RF frequency and power. The PES-LIG membrane's mechanical and thermal properties are characterized to investigate its feasibility for MD application. In this work, vacuum MD (VMD) is studied by integrating RF heating and permeate flux up to 13.5 $Lm^{-2}h^{-1}$ with >99% salt rejection is reported. Cyclic thermal and mechanical stability tests and long-term VMD tests show stable performance of the PES-LIG membranes. This work demonstrates a novel MD technique strategy that can potentially address challenges impeding its commercialization.

Keywords: radiofrequency, membrane distillation, laser induced graphene, surface heating, membranes

1. Introduction

Global freshwater scarcity is a pressing issue that emphasizes the critical need for more efficient desalination technologies,[1] especially those that can be applied to brine streams with high salinity. Membrane distillation (MD) is an emerging desalination technique that can treat hypersaline brine (salinity greater than 75,000 ppm);[2] it is a thermally driven process, in which the temperature difference between the feed and the permeate sides induces the partial vapor pressure gradient across the membrane and leads to permeation of the water vapor molecules through a microporous membrane.[3] MD membranes are hydrophobic; hence they only allow vapor to pass through the membrane pores whereas liquid water is being repelled. The vapor that transfers to the permeate side is condensed and collected as pure distillate. MD is advantageous over other techniques as it requires a lower operating temperature, and reaching to water boiling temperature is not necessary;[4] this makes MD a viable choice for integration with renewable or waste heat.[5] MD is also less prone to fouling due to the hydrophobic nature of the membrane. MD also has the potential to be more energy-efficient at smaller scales.[6] In addition, 100% theoretical rejection for non-volatile compounds makes it even more interesting, especially for near-zero liquid discharge applications.[7]

For the target use in water recovery from hypersaline brine, there are yet two withstanding challenges for MD, which impede deployment at scale: scaling and energy intensity.[6] Major efforts have been dedicated to mitigating scaling/fouling by tailoring membrane properties through enhancing the hydrophobicity.[8, 9] Teoh et al. used polytetrafluoroethylene microparticles in the polyvinylidene fluoride (PVDF) polymer solution, which displayed improved hydrophobicity (contact angle around 130°).[10] Edwie et al. also reported PVDF membranes blended with fluorinated silica particles, which displayed contact angles as high as 139.84°.[11] Functionalizing the membrane surface has also shown enhanced membrane properties for MD applications.[12, 13] While innovations in designing MD membranes display an ever-increasing momentum, there are fewer opportunities being explored to improve the energy efficiency of MD. The heat loss due to the conduction through the membrane and latent heat of evaporation results in temperature decline on the membrane surface compared to the bulk feed temperature,[14] which is referred to as temperature polarization (TP).[15] Continuous evaporation of water from the feed side also leads to increased salt concentration on the membrane surface, thereby reducing the partial vapor pressure

gradient across the membrane, also known as concentration polarization (CP).[15] Both TP and CP reduce temperature and vapor pressure gradient across the membrane, which eventually deteriorates MD performance and makes it more energy intensive. An interesting approach to improve energy efficiency and reduce scaling is designing surface-heated membranes, in which only the feed in contact with the membrane at the mass transfer interface is heated. This heating approach replaces complex external heating of bulk fluid. The surface heating concept not only has the potential to lower the energy requirement, but also improves MD performance.[16] Compared to conventional bulk feed heating, surface-heated membranes have the promise of reducing the costs while simplifying the unit operations in large scale MD applications.[16-20]

To date, the membrane surface heating concept is mostly integrated into MD through photothermal, Joule, and inductive heating approaches.[17, 18, 20-22] In photothermal heating, functional materials are incorporated into the membrane that converts solar energy to thermal energy on the membrane surface and at the mass transfer interface.[19, 21, 23-26] However, the intermittent nature of solar energy and relatively high costs of such membranes are considered as major challenges for photothermal heating.[27] Joule/induction heating of electroconductive membranes are independent of any intermittency. However, Joule heating involves electrodes to be in contact with brine which corrodes during MD operation.[28] With induction heating, although the heating coil is not in contact with the salt water, it involves a complex design of the heating coil to make it compatible with the MD module.[16] A simpler and unexplored approach for membrane surface heating is using radiofrequency (RF) or microwave based electromagnetic heating which do not require the applicator/electrode to be in direct contact with the brine feed. For membrane surface heating, RF is advantageous over microwave because of its lower frequency range, which offers safer operation and higher penetration depth that helps with more uniform heating of thick materials[29]. This makes RF an excellent alternative over Joule, induction, and microwave heating for membrane surface heating in MD applications.

Electroconductive characteristics are typically introduced to the polymeric membranes with the incorporation of carbonaceous materials, i.e., graphene, graphene oxide (GO), CNT, activated carbon, etc., which are more popular than other materials (i.e., metal nanoparticles) because of their excellent conductivity, mechanical stability, and chemical robustness.[2, 4, 12-14] The synthesis and incorporation of electroconductive materials involve handling harsh chemicals, expensive

equipment, and are not quite feasible for large-scale manufacturing.[30, 31] For instance, CNT is widely used to fabricate electroconductive membranes, which relies on complicated manufacturing techniques like chemical vapor deposition, arc discharge, etc. resulting in expensive membrane fabrication.[32] Carbonaceous materials are hydrophobic in nature, but the presence of functional groups like -OH, -NH_2, -COOH makes them hydrophilic, which would require further modification for MD application.[33] Therefore, a simple new hydrophobic electroconductive membrane preparation technique is of interest.

An interesting approach that has been explored recently to prepare electroconductive membranes is laser-induced graphene (LIG).[28, 34, 35] In this technique, an infrared or ultraviolet laser source is used to convert a polymer substrate into graphene through a photothermal reaction.[36] High localized temperature is generated; the laser pulse irradiates the polymer substrate and breaks the chemical bonds of functional groups with the aromatic backbone to obtain an interconnected multilayered graphene with 3D porous structure.[37] Laser-induced formation of multi-stacked graphene on the membrane surface is of particular interest, compared to other carbon derivatives, because of its chemical-free, facile, single-step, and scalable process that can be operated in ambient conditions without any pre- or post-treatment.[36] A unique advantage of laser ablation technique is that the surface wetting properties can be tuned through controlling the lasing parameters. Tour et al. have shown that controlling the lasing environment resulted in the formation of hydrophobic LIG surface.[38, 39] Hydrophobic LIG membrane was synthesized in our work using a new lasing approach. This is also the first time that the use of RF-heated hydrophobic electroconductive LIG membranes is being reported for surface heating concept in MD application.

In this work, we fabricated novel hydrophobic electroconductive LIG membranes based on polyethersulfone (PES) membrane substrate. Hydrophobic LIG surface with tunable properties was fabricated by optimizing the lasing parameters to prepare electroconductive MD membranes. The structure and properties of the membrane was studied via various characterization techniques to confirm that membrane properties are suitable for MD application. Thermal performance of the LIG membranes was studied using RF heating technique; RF parameters were first optimized, and further experimentation was carried out to explore the surface-heating properties of LIG membranes. Finally, RF heating of LIG membranes in short- and long-term vacuum MD (VMD) tests were evaluated to gain insights into the performance of the fabricated membranes. Our study

reports the first demonstration of RF surface heating of electroconductive LIG membrane, studied here for MD applications.

2. Results and Discussion

2.1. LIG MD Membrane Fabrication

We synthesized PES membrane substrates (hereafter referred to as substrate) via nonsolvent-induced phase separation (NIPS) technique (Figure 1a). An extra step was added to the NIPS. The substrate was soaked in the $CaCl_2$ solution as depicted in the outline of the synthesis process. This step was critical to preserve the pores of the membrane upon drying and lasing. CO_2 laser ablation was then applied on the substrate surface. To successfully conduct MD filtration tests, having a hydrophobic surface that can withstand wetting in long-term tests is a necessity. Additionally, the pore size should be within a reasonable range (<0.5 μm) to achieve reasonably large liquid entry pressure that can sustain the mass transfer interface on the membrane side. The most important consideration in making LIG membranes for MD is to preserve membrane microporous features upon laser induction. Photothermal laser ablation induces temperatures above 2500 °C on the substrate surface that can cause graphitization of polymer substrate.[40] This laser irradiation process photothermally convert sp^3-carbon atoms to sp^2-carbon atoms followed by releasing the functional groups as gas while the remaining aromatic compounds transform to graphene.[41] For the PES membrane substrate, this graphitization process is illustrated in Figure S3 that happens by dissociating bond of functional groups (-SO_2, -O-) at high temperature. Tuning the interactions of the laser and polymeric substrate is a sophisticated task because if the laser parameters are not carefully chosen based on substrate properties, it will distort the membrane structure. If not enough power is applied, it can melt the membrane at the laser contact point and destroy the substrate's porous structure, which eventually decreases the membrane permeability.[42] Increased laser power, on the other hand, delivers higher power to the substrate surface and engraves deeper, hence leading to a greater conversion of PES to graphene.[34] In an excessive case, lasing can lead to uncontrolled sintering of the substrate and formation of defects (large pores) that will immediately result in membrane wetting. Therefore, we focused on the following three goals that need to be achieved when making PES-LIG membranes for MD application: *i)* the membrane surface must be hydrophobic, *ii)* an interconnected 3D porous graphene layer susceptible to RF signals is

required, *iii)* and membranes must be defect-free. To achieve these goals, it is necessary to carefully select laser parameters for the ablation of substrate.

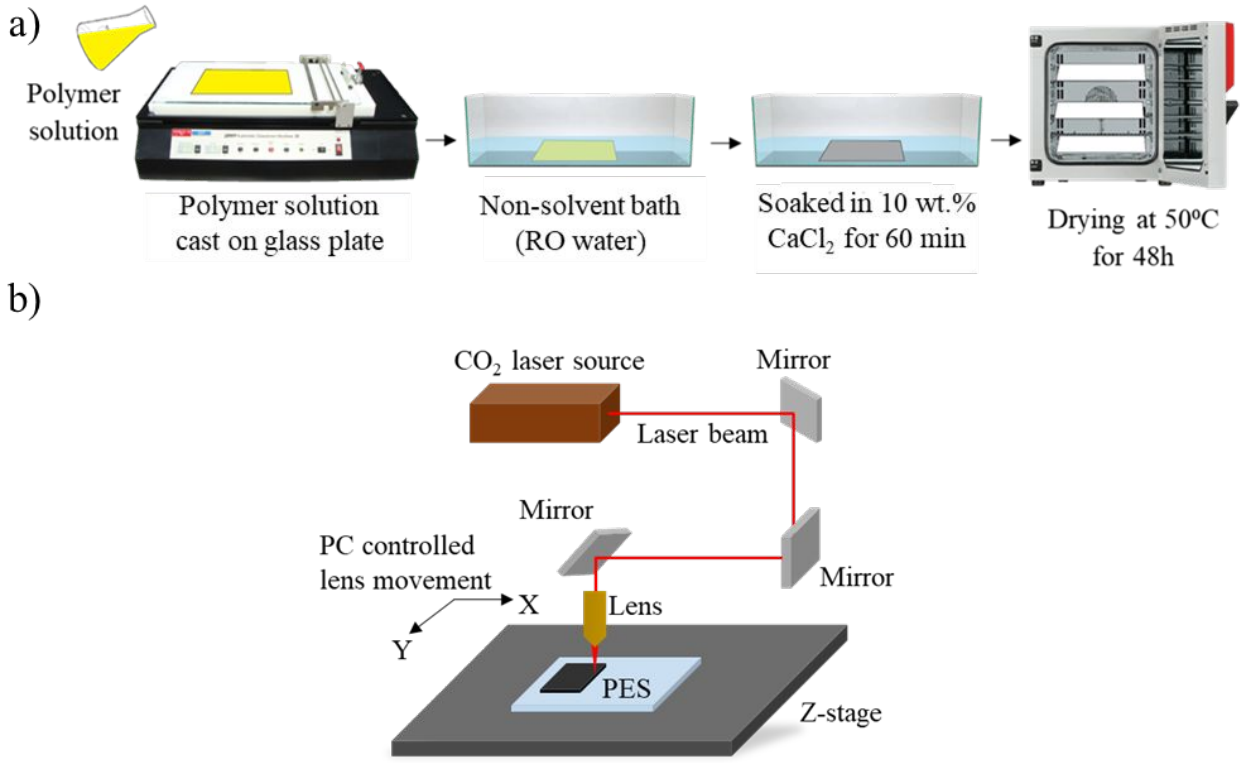

Figure 1. **a)** Schematic of the PES membrane substrate fabrication process. **b)** CO_2 laser ablation technique.

A typical schematic of laser ablation process is shown in Figure 1b, where the laser can move in both x and y directions on the substrate. Key parameters that control the substrate scribing are laser scanning mode (raster vs. vector), power, speed, PPI, and lines per inch (LPI), which can extensively influence the quality and distribution of LIG 3D structure.[37] For the laser scanning, vector mode with a cross-hatch pattern was preferred over raster mode, because it resulted in formation of a hydrophobic LIG surface on the substrate in the air-assist mode[39] – without the need to have a controlled environment.[43] We could tune vector mode lasing by varying the power, PPI, and speed, while we found lasing to be less influenced by LPI (refer to Section S3 of Supporting Information for details). Laser power was tuned to control the LIG density; an increased laser power engraved deeper into the substrate. Higher PPI resulted in an increased number of laser pulses, which increased graphene density on the PES membrane substrate.[37] Laser speed controls the time that any spot on the substrate will be exposed to the laser beam. This

indicates that higher laser speed would lead to lower PES conversion to graphene. After a careful optimization of lasing parameters, PPI and speed were set at 1000 PPI and 40%, respectively, while power was varied between 1% and 14%. PPI was kept constant at its highest value of 1000 to obtain higher LIG density which will enhance the RF heating response.

It is imperative to tune lasing parameters to obtain a hydrophobic LIG surface. Results in Figure 2a and b show that PES membrane substrate prepared via NIPS displayed an equilibrium contact angle close to ~60° (laser power 0 W in Figure 2a and b). Previous reports on using laser ablation for graphene formation primarily focused on the raster mode lasing, which results in the formation of hydrophilic surface in air.[34, 43] As shown in Figure 2a and b, we successfully demonstrated the formation of a hydrophobic surface on the PES membrane substrate by lasing in the vector mode. Variation in the laser power was found to be the major parameter that substantially changed the wetting properties of the surface. With the increase in the laser power, the equilibrium water contact angle for both PES-LIG-18 and PES-LIG-22 membranes increased (results for PES-LIG-16 and PES-LIG-20 are shown in Figure S5a and b of Supporting Information). At lower laser power (1% - 3%), the conversion of PES to graphene was low. Figure S6 shows digital images of laser-ablated PES membrane substrates having higher graphene formation with increasing laser power. When the laser power is not high enough, carbonization does not occur (Figure S6, for laser power 1% and 2%, Video S1 and S2). The dynamic contact angle is also reported, which shows both advancing and receding water contact angles at higher laser power in the hydrophobic range. To explain this, it should be noted that during the laser irradiation, the photothermal induced reaction creates localized high temperature on the polymer surface.[44, 45] As a result, functional groups like ether and sulfonyl in the PES membrane substrate decompose, hence, carbonizing the aromatic backbone. It has been reported that the basal plane of graphene usually contributes to hydrophobicity, whereas the edge shows hydrophilic properties due to the presence of defects.[39, 43] We hypothesize that implementing laser ablation in the vector mode enhances the exposure of the graphene basal plane that shows increased hydrophobicity on the substrate. For further study, laser power showing the highest water contact angle for each specific PES-LIG membrane was chosen unless otherwise stated which is summarized in Table S1 of Supporting Information.

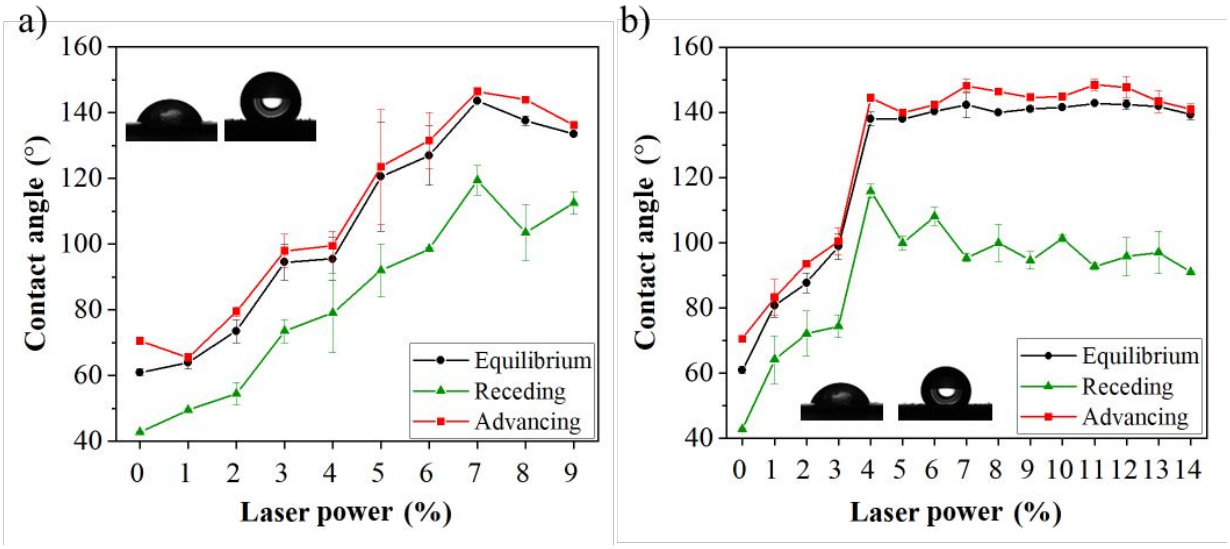

Figure 2. Water contact angles (equilibrium and dynamic) for **a)** PES-LIG-18, and **b)** PES-LIG-22 membrane surfaces. (Image insets in **a** and **b** display the sessile drop images for minimum and maximum water contact angles.)

2.2. LIG Characterization

SEM images displayed in Figure 3a and d suggest that a highly interconnected 3D LIG was formed on PES-LIG-18 and PES-LIG-22 (refer to Figure S5c and d for PES-LIG-16 and PES-LIG-20, respectively). LIG is formed along the cross-hatch path with 1/72" spacing. Cross-section SEM images were also taken as displayed in Figure 3b and e, which confirm the preserved microporous structure of PES-LIG-18 and PES-LIG-22, respectively, while a relatively thick 3D LIG layer is formed on the membrane surface. It is important to note that choosing the right side of the membrane substrate for laser ablation is critical as the membrane substrate structure is asymmetric. A detailed discussion on lasing side selection is provided in Section S6 of Supporting Information. From the cross-section SEM image in Figure 3b and e, approximately 20% (Figure 3b) and 35% (Figure 3e) of the PES membrane substrates are converted to LIG, and the rest is preserved with finger-like porous structure. Interestingly, at the same laser power for the substrate treated without immersion in $CaCl_2$ solution, the whole membrane thickness was burnt, destroying the membrane microstructure (cf. Figure S8). Soaking in $CaCl_2$ had two major impacts. Primarily, pore filling with $CaCl_2$ was found to be effective in avoiding the collapse of porous structure in the drying stage of the phase inversion. He et al.[46] showed that soaking the membrane in $CaCl_2$ could retain 97% of the wet flux for the PES ultrafiltration membrane. Additionally, we demonstrate that the presence of $CaCl_2$ assists with protecting the membrane's porous features upon lasing. We

hypothesize that $CaCl_2$ diminishes the heat transfer across the membrane; it acts as heat shield that protects the soft polymeric PES membrane substrate. The uniform distribution of Ca through the porous membrane matrix is confirmed and illustrated in Figure 3c and f. EDS mapping of Cl is also shown in Figure S9 of Supporting Information, which shows a similar distribution in the cross-section of the membrane.

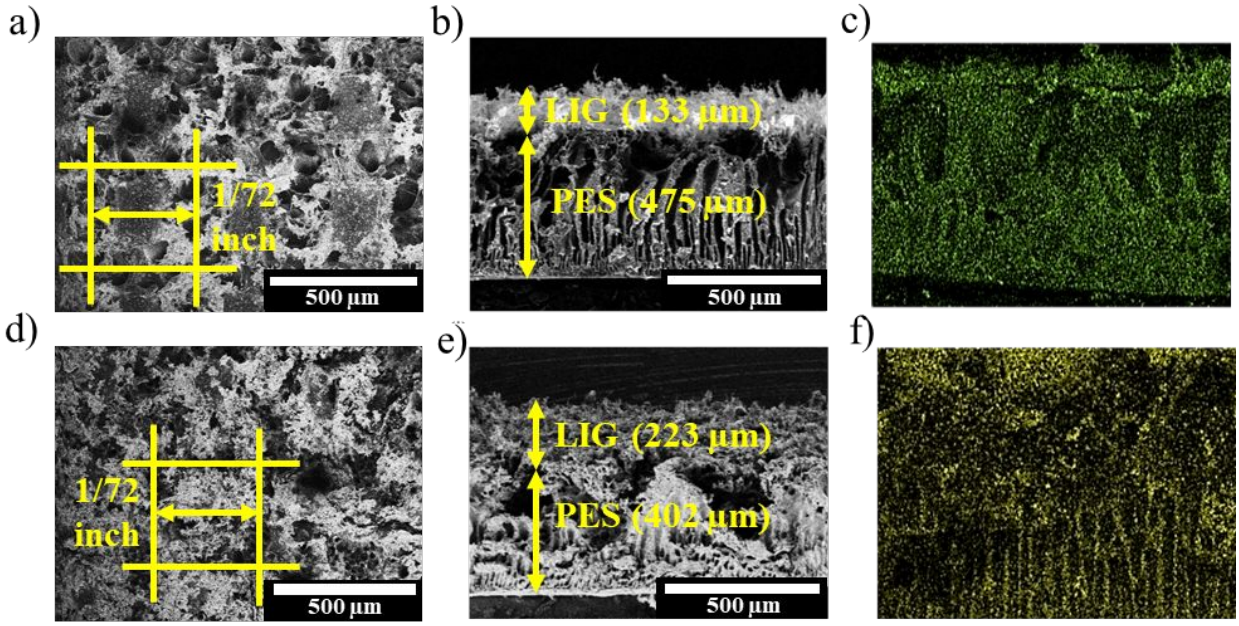

Figure 3. **a, d)** SEM images of PES-LIG-18 and PES-LIG-22 membrane surfaces, respectively. **b, e)** cross-section SEM images of PES-LIG-18 and PES-LIG-22 membranes, respectively. **c, f)** EDS mapping of Ca in the cross-section of PES-LIG-18 and PES-LIG-22 membranes, respectively.

The formation of graphene under laser ablation was evaluated with TEM imaging which shows LIG texture at the nanometer scale (Figure 4a and b) and multilayer graphene with wrinkles on a two-dimensional plane. The high-resolution TEM in Figure 4b shows graphene layers that display 3.5 Å lattice spacing, which is in agreement with earlier reports.[36, 47, 48] This is an indication for the successful formation of graphene with the lasing conditions used on PES membrane substrate. Raman analysis, being the primary evidence for the formation of LIG, was also studied on the laser-ablated PES Membrane substrate. Characteristic graphene peaks in Raman spectra are D, G, and 2D peaks at ~1350, ~1580, and ~2700 cm^{-1} wavenumber.[41] Figure 4c shows distinct D and G peaks, observed for PES-LIG-16, PES-LIG-18, PES-LIG-20, and PES-LIG-22 membranes, whereas no strong 2D peak was obtained due to the short height of 2D peak compared to the

background noise. There are two major reasons for the weak 2D peaks. First, graphene formed in the vector mode with 1/72" spacing does not form a continuous graphene layer. Thus, a major portion in between the continuous LIG medium is the exposed surface of the PES membrane substrate. Second, the 2D peak in Raman displays the largest intensity for single-layer defect-free graphene, while graphene formed upon laser ablations has a defective multilayer structure, which results in the broadening and disappearance of the 2D peak for graphene. As a result, the absence of a strong 2D peak should not be interpreted as the absence of graphene.

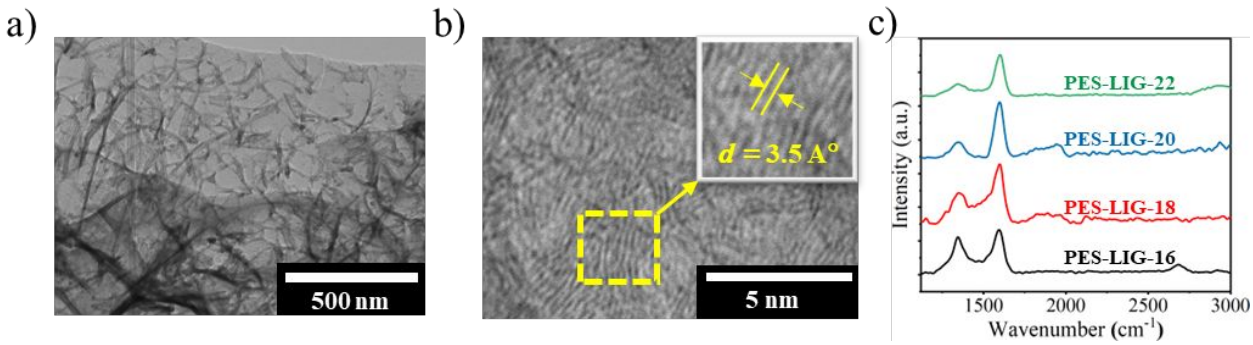

Figure 4. a, b) TEM images of PES-LIG-22 membrane. **c)** Raman spectra of PES-LIG membranes produced from different PES membrane substrates.

The elemental composition of PES membrane substrate and LIG was studied with XPS to confirm the graphitization of PES membrane substrate under laser ablation using PES-LIG-22 membrane. Since a cross-hatch pattern lasing template was used that results in graphitization along the laser path, XPS beam diameter of 50 μm was used to avoid interference from the nearby PES area as much as possible – although inevitable. The survey spectrum in Figure 5a for PES-LIG-22 membrane on PES and LIG suggests the presence of C, O, S, Ca, and Cl. However, with the formation of LIG after laser ablation, carbon content increased from 76.7% to 87.1%. At the same time, O and S contents decreased, which confirms graphitization of the PES membrane substrate. Ca and Cl content decreased significantly after laser ablation confirming the role of $CaCl_2$ only in protecting the PES membrane substrate during laser ablation. Detailed elemental composition obtained from survey spectra is summarized in Table S2. High-resolution C1s and O1s spectra are shown in Figure 5b and c for LIG, and Figure S10a and b for PES membrane substrate. For both LIG and PES, the C1s peak was deconvoluted into 284.7, 286.3, and 291.8 eV corresponding to C-C/C-H, C-O, and π-π*, respectively. O1s peak was deconvoluted into two peaks at binding energies of 531.9 and 533.2 eV for O=S=O and O-C, respectively. Higher peak intensity of C-

C/C-H and lower peak intensity of C-O in LIG compared to the PES membrane substrate verify the highly carbonized structure of the LIG membrane on the surface. Similarly, in the O1s deconvoluted peaks, peak intensity for O=S=O decreased in LIG compared to the PES membrane substrate, which further confirms the conversion of PES to LIG under laser ablation.

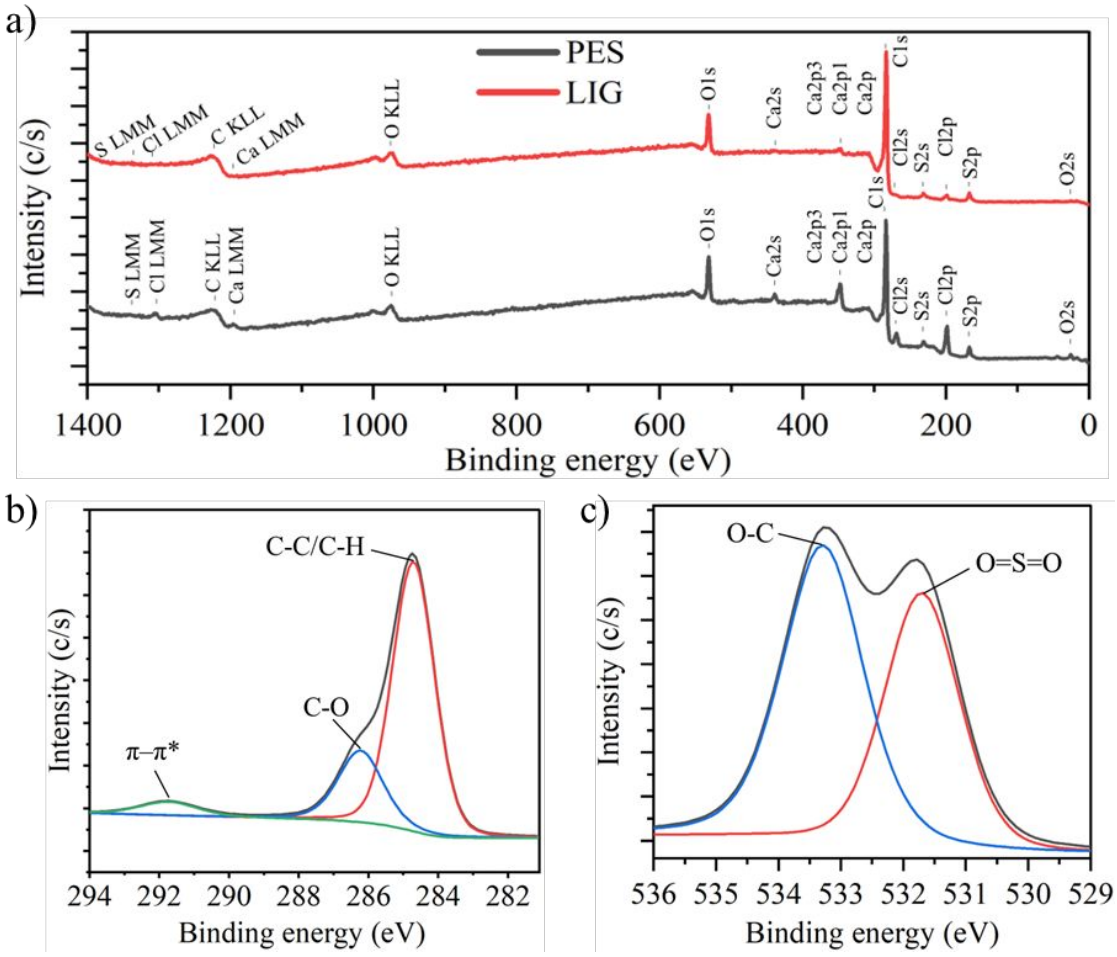

Figure 5. a) XPS survey spectrum for PES and LIG on PES-LIG-22 membrane. **b)** C1s and **c)** O1s high resolution spectra of LIG of PES-LIG-22 membrane.

Nitrogen physisorption on 3D porous LIG samples derived from PES-LIG-18 and PES-LIG-22 disclose interesting findings regarding PES-LIG membrane pore size distribution. For PES-LIG-18 membrane, pore volume of 1.35 cm^3/g and BET surface area of 5.9 m^2/g were obtained from our measurements. In the case of 18% bare PES membrane substrate, pore volume and BET surface area were 0.06 cm^3/g and 4.95 m^2/g, respectively. This proves that the formation of LIG increased the overall pore volume and surface area of the PES-LIG membrane. Similar observation was found for PES-LIG-22 membrane, as results summarized in Table S3. LIG formed on the

membrane surface displayed a bimodal pore size distribution as shown in Figure 6. The first portion of the porous structure with average pore size of ~5 nm belongs to the microporous structure of graphene formed with laser ablation.[41] This bimodal distribution is not observed for the pore size distribution of bare PES membrane substrates shown in Figure S11 of Supporting Information due to the absence of the microporous graphene. For PES-LIG-18 membrane, another strong peak was observed with pore size of 60-70 nm (Figure 6a), which can be attributed to the porous structure of the PES membrane substrate. However, for the PES-LIG-22 membrane (Figure 6b), this shifted toward smaller sizes of 30-40 nm, which is expected as higher polymer dope concentration can result in tighter PES membrane substrate formation via NIPS.

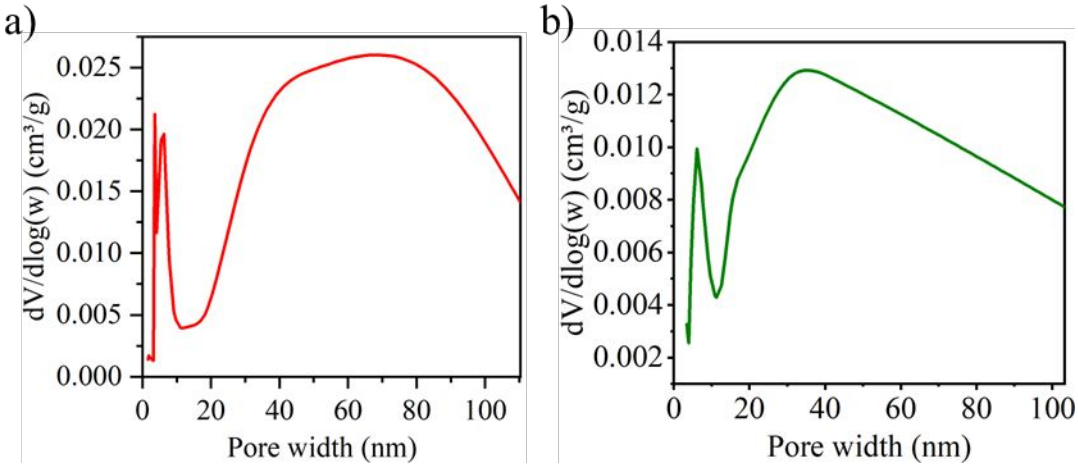

Figure 6. Pore size distribution of **a)** PES-LIG-18, and **b)** PES-LIG-22 membranes.

Mechanical and thermal robustness of the LIG membrane is critical for the longevity of MD application. Uncontrolled lasing can deteriorate membrane mechanical stability. Additionally, fast thermal responses in RF field necessitate the LIG membrane to be thermally stable. Tensile tests were used to evaluate the mechanical strength of the PES membrane substrate before and after laser ablation, and results are displayed in Figure 7a and b. Before lasing, tensile strength for the PES membrane substrates ranged from 5.0 to 6.8 MPa, whereas after lasing, it slightly decreased to 3.85-4.35 MPa. The decline in tensile strength can be attributed to the reduced thickness of the PES membrane substrate due to laser ablation. Thakur et al. reported a similar observation for the tensile strength of the LIG membranes that were successfully used for filtration.[34] For the thermal stability study, TGA of the LIG membranes was carried out, and results are displayed Figure 7c.

Other than weight loss due to the removal of the moisture content at temperatures up to ~120 °C, the membrane displayed satisfactory stability at temperatures as high as 500 °C. A similar observation was found in the TGA of bare PES membrane substrate, as shown in Figure S12 of Supporting Information. For further characterization and experimental studies, we downselected to PES-LIG-18 and PES-LIG-22 to simplify experimental design.

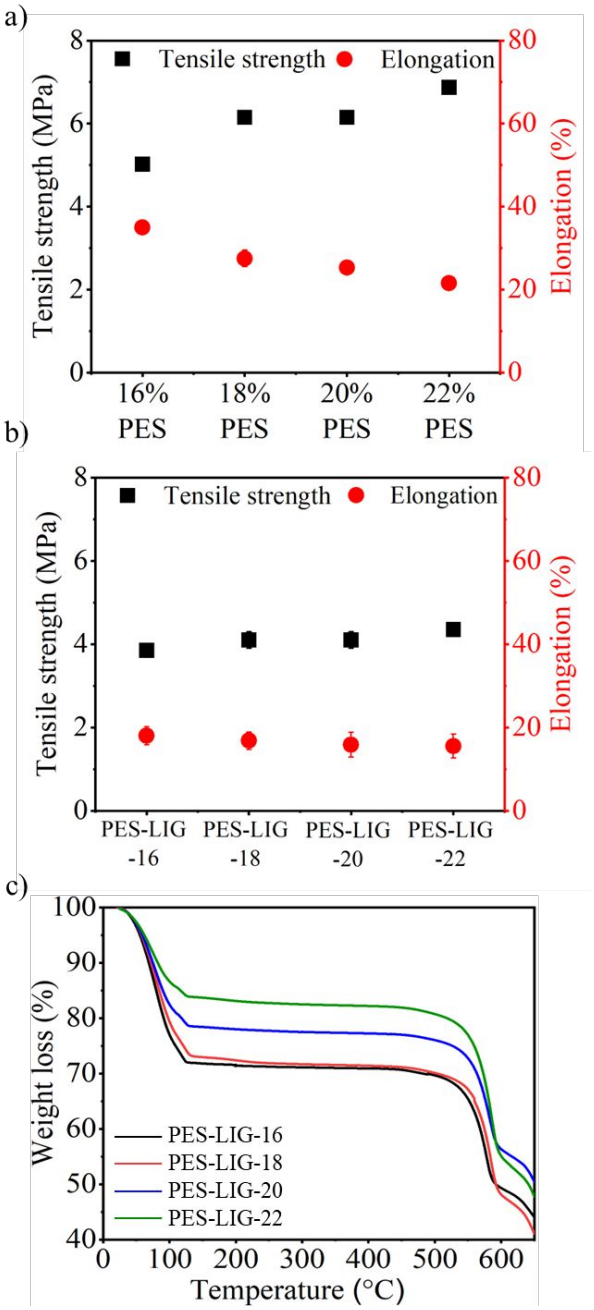

Figure 7. a) Mechanical strength of PES, and **b)** PES-LIG membranes. **c)** TGA analysis of PES-LIG membranes. Note: the error bars for PES membrane substrate are small so it is not easily visible.

2.3. RF Heating and Thermal Properties of PES Membrane

After successful fabrication of PES-LIG membranes, RF heating performance was evaluated. Figure S1a shows simple schematic of an RF heating setup where the LIG sample was placed over an applicator (Figure S1b), and a forward-looking infrared (FLIR) camera was used to capture the thermal response. RF field response is highly influenced by the sample's electromagnetic properties, applicator design, as well as surrounding environment. In this work, reflection coefficient measurement experiments were carried out to find the frequency that can result in minimal signal loss due to reflection with our membrane assembly. The schematic of the reflection coefficient measurement setup is shown in Figure S1c.

Reflection coefficient measurements were performed using PES-LIG-18 in different scenarios to evaluate the RF field response in the frequency range of 50 to 350 MHz, and results are displayed in Figure 8. Low reflection coefficient is the result of a low impedance mismatch, which is necessary to maximize the RF power delivered to the membrane. Four different feed-permeate combinations within the membrane module were studied: *i*) no feed and no vacuum (NFNV), *ii*) no feed with vacuum on the permeate (NFV), *iii*) feed circulation and no vacuum (FNV), *iv*) both feed circulation and vacuum present (FV). For NFNV condition, the lowest reflection coefficient is at ~100 MHz. When vacuum was pulled on the permeate side, air started flowing through the LIG and pores of the membrane, and hence the response to the RF field changed (shifting the lowest reflection coefficient to ~80 MHz). When only feed water was circulated, the lowest reflection coefficient was found at ~180 MHz. This proves that the presence of saline water influences the RF field response significantly. Finally, when vacuum was pulled while keeping the feed water circulation (FV), a different response of the reflection coefficient was found with the minimum reflection coefficient at ~91 MHz. Our interest is to find the frequency at which the minimum reflection coefficient is obtained for the FV scenario, as it best represents the actual filtration in the VMD configuration. Evidently, the reflection coefficient again started decreasing beyond 220 MHz for the FV condition, which might decrease further beyond our selected frequency range. However, we decided to limit the frequency below 200 MHz as it is safer for

operation; additionally, lower frequency leads to higher penetration depth, which is more efficient for bulk heating.[29] Thus, we selected 91 to 200 MHz to study VMD performance in the RF field.

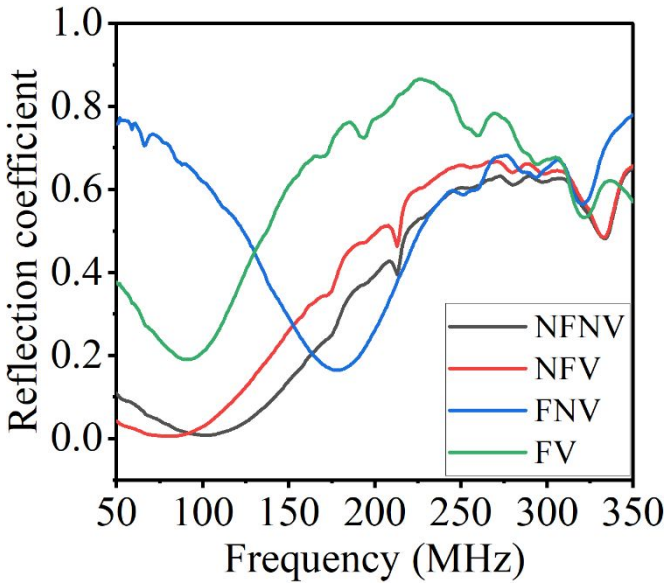

Figure 8. Reflection coefficient at different feed-permeate combinations in the membrane cell for PES-LIG-18 membrane.

After identifying the optimum frequency range, the thermal responses for the PES-LIG membranes were tested. A representative thermal response for the membrane is shown in Figure S13. The temperature reported in different results from FLIR response was calculated by taking the average temperature from the surface of the membrane active area. Figure 9a shows the average surface average temperature of the PES-LIG-18 and PES-LIG-22 membranes at different RF powers and frequencies. The power is represented in the x-axis in terms of amplifier gain. This parameter is used for the ease of comparison among the membranes. The relationship between amplifier gain to the input power is provided in Figure S14. Results indicate that among the three different frequencies applied, 91 MHz gives the highest surface temperature, which corroborates our observation in the reflection coefficient experiments. For 150 and 200 MHz, the reflection coefficient increases which leads to reduced input power and thereby lower surface temperatures. Figure 9a also shows the effect of RF power (amplifier gains 0%, 5%, and 10%) on the surface temperature for the three different frequencies. It is important to mention that gain 0% does not mean that RF input power was 0 W; instead, it indicates the amplifier's minimum gain setting (with 100% indicating the amplfier's maximum gain setting). In our case, amplifier gain 0% refers to an input power of ~3-6 W, as shown in Figure S14. As expected, results confirm that higher

surface temperature is achieved when increasing the amplifier gain. These experiments were carried out in ambient conditions with LIG surface exposed to air to allow temperature measurement with FLIR camera. Thermal response for amplifier gains beyond 10% is not reported as the membrane surface temperature of PES-LIG-22 reaches beyond glass transition temperature of 225 °C and PES membrane substrate starts losing its mechanical stability. Results also suggest that the surface temperature for PES-LIG-22 was always higher than PES-LIG-18 membrane, which can be attributed to the higher graphene content in PES-LIG-22 membrane confirmed by SEM images.

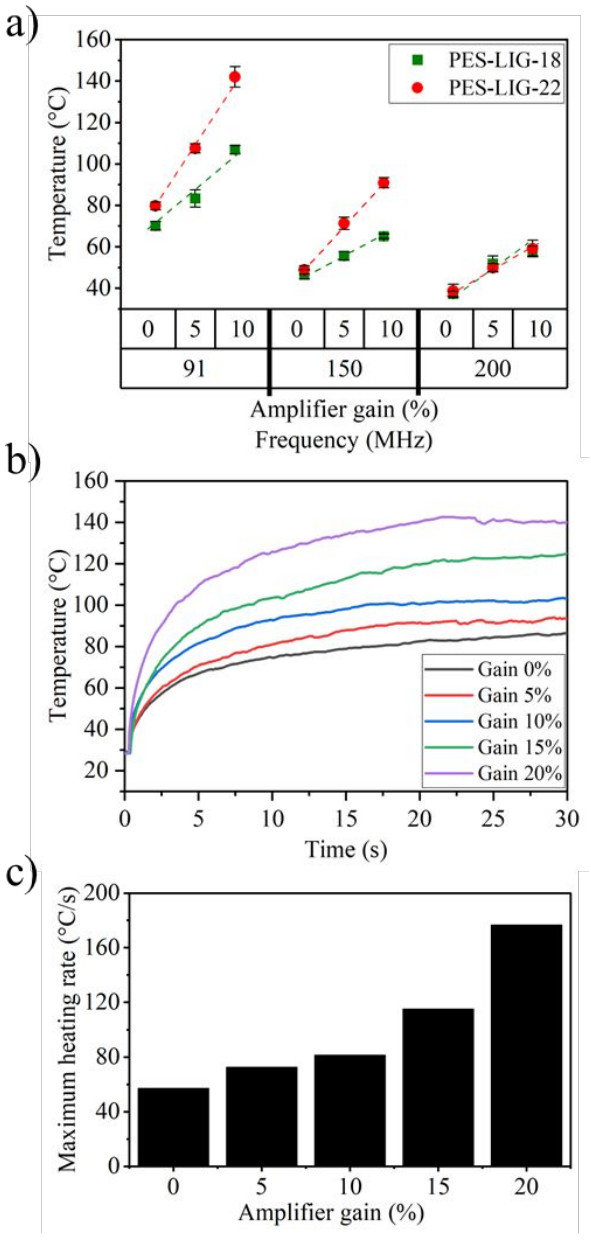

Figure 9. **a)** Thermal responses of PES-LIG-18 and PES-LIG-22 at different RF input power (0-10 W) and different frequencies. **b)** Transient thermal response for PES-LIG-18 at various gains. **c)** Maximum heating rate from the transient thermal response for PES-LIG-18. Both results in b and c are obtained at 91 MHz.

The transient thermal response for different amplifier gains in the range of 0-20% is displayed in Figure 9b. Within 15-20 seconds, the membrane surface temperature reaches 120 ℃. Such fast response is another advantage over conventional MD with external heat exchanger network that requires longer startup time to reach close to steady state condition. Over this period of transient thermal response, the maximum heating rate for the LIG membrane was also studied which is shown in Figure 9c. With increasing amplifier gain, the heating rate increases. For the highest applied power (20% gain), the maximum heating rate of 180 ℃/s is recorded. This demonstrates the promising RF heating characteristic of PES-LIG membranes for MD application.

Thermal stability for long-term MD operation is another necessity for the commercial application of PES-LIG membranes. To investigate if the PES-LIG membrane used in this work can withstand fast cycles of RF heating for a long period of time, cyclic thermal stability tests were investigated, and thermal response results are provided in Figure 10a (PES-LIG-18 membrane with amplifier gain of 20%). To manage the number of experiments, we selected PES-LIG-18 as the model membrane for the cyclic thermal stability test because of its improved flux while withstanding high laser power to form sufficient graphene on the PES-LIG membrane surface. For 20 cycles, the total time for the experiment was approximately 8 h, and in each cycle, temperature was found to be stable and close to 150 ℃. This confirms that PES-LIG membrane prepared in this work has stable and reproducible thermal response to RF signals. For each cycle, maximum heating rate was also calculated (Figure 10b). Maximum heating rates in the range of 150 to 180 ℃/s were also obtained.

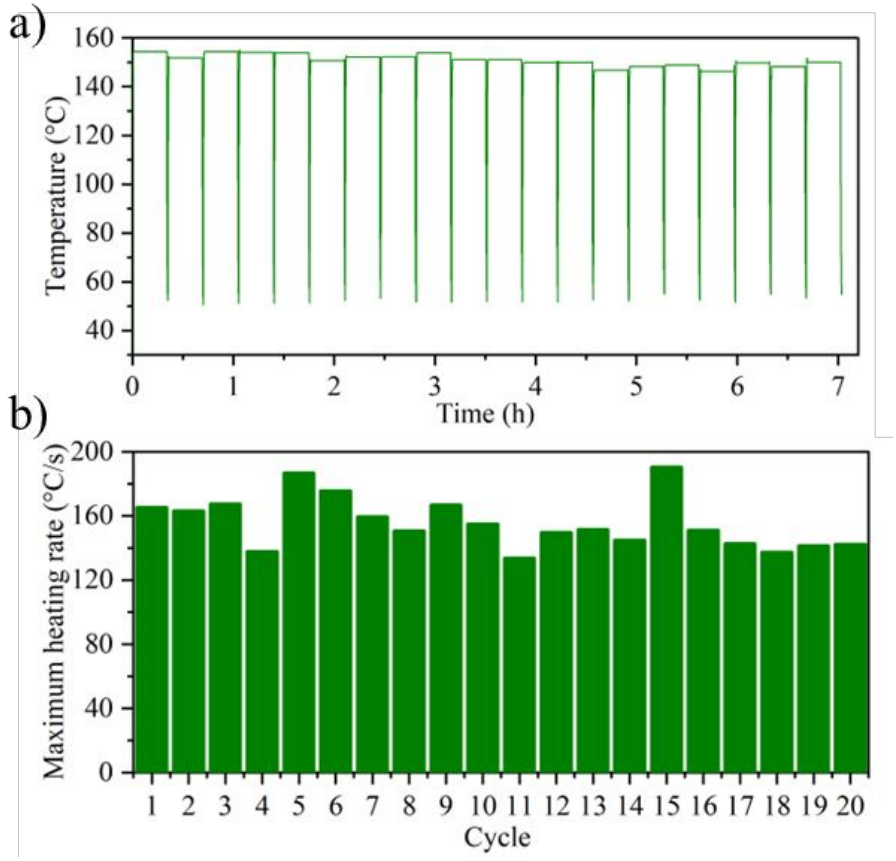

Figure 10. **a)** Cyclic thermal stability test, and **b)** maximum heating rate for PES-LIG-18 at 91 MHz and gain 20%.

2.4. MD Performance of LIG Membrane in RF Field

The MD performance of PES-LIG membranes with surface heating was evaluated using a custom-built VMD setup integrated with RF heating. Details of the experimental setup are shown in Figure S2 of Supporting Information. The conventional and the RF surface heating concept in MD are shown as schematics in Figure S15a-c. For conventional MD experiments, an external heat source is required to heat the brine (Figure S15a), whereas no external heat source for bulk fluid heating was necessary for RF-heated MD (Figure S15b). Figure S15c shows the enlarged image of the PES-LIG membrane with the RF applicator.

VMD experiments with RF heating were conducted to evaluate the performance of PES-LIG-18 and PES-LIG-22 membranes. To study the efect of RF input power, RF amplifier gain was varied from 0 to 20%. As shown in Figure 11a and b, increasing RF input power led to enhanced permeate flux for both membranes, which is expected as the energy delivered to the membrane surface

increases. We also ran VMD with the PES-LIG membranes without surface heating for comparison with RF-heated VMD. For PES-LIG-18 and PES-LIG-22 membranes, flux was 0.7 L m^{-2} h^{-1} and 0.3 L m^{-2} h^{-1}, respectively, which are significantly lower than RF heated VMD with the lowest RF power (amplifier gain 0%) used in this work. In terms of the frequency, the permeate flux for both PES-LIG-18 and PES-LIG-22 membranes decreased with increasing the RF frequency, keeping other parameters constant. The highest flux achieved for PES-LIG-18 and PES-LIG-22 membranes were 13.5 L m^{-2} h^{-1} and 9.1 L m^{-2} h^{-1} at 91 MHz, and the lowest flux was found at 200 MHz. This agrees with our observation from the reflection coefficient measurements discussed earlier.

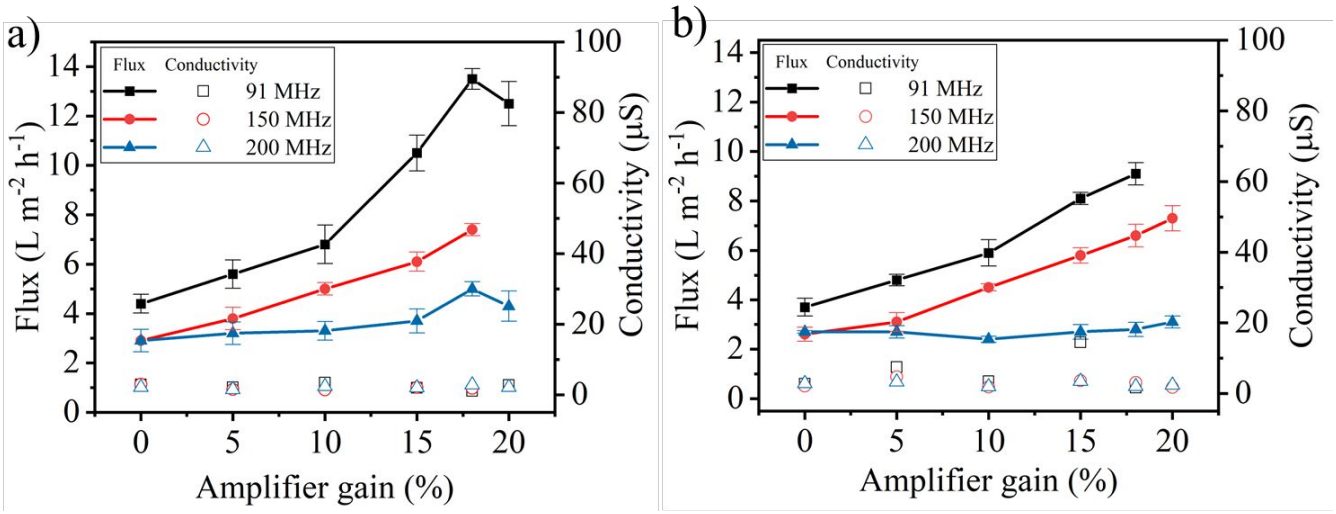

Figure 11: a) Effect of amplifier gain on the MD performance of various membranes – namely **a)** PES-LIG-18, and **b)** PES-LIG-22 membrane – at different RF frequencies.

Membrane made with different laser power was used in VMD experiment to investigate the role of laser power. We fabricated membranes with laser power of 5 to 7% for PES-LIG-18 and 9 to 11% for PES-LIG-22 membranes. For both PES-LIG-18 and PES-LIG-22 membranes, VMD flux increased with increasing the laser power, as shown in Figure 12a and b, respectively. Previously, we discussed that higher laser power gives a higher graphene density and a higher water contact angle on the surface of PES-LIG membranes. For similar RF input power, higher graphene content leads to increased surface temperature and more uniform temperature distribution, thereby enhances the MD's driving force. However, deviation in the increasing trend of flux result is observed for PES-LIG-18 membrane with 0% amplifier gains, where the flux for laser power 7%

was lower compared to laser power 6%. This can be attributed to the the presence of wrinkles (Figure S16) on PES membrane substrate prepared in phase inversion technique resulting uneven surface that may result in nonuniform LIG formation during laser ablation, thus, resulting in reduced flux. In the case of PES-LIG-22 membranes, a smoother membrane surface was obtained, which results in formation of a more uniform LIG surface under laser ablation and permeate flux increases with increased laser power. For the PES-LIG-22 membrane in Figure 12b, flux data for 20% amplifier gain (membrane made with laser power 9,10, and 11%), and 18% amplifier gain with laser power 11% has not been reported as the membrane started melting in RF field. This resulted in immediate membrane wetting, leading to permeate conductivity similar to the feed.

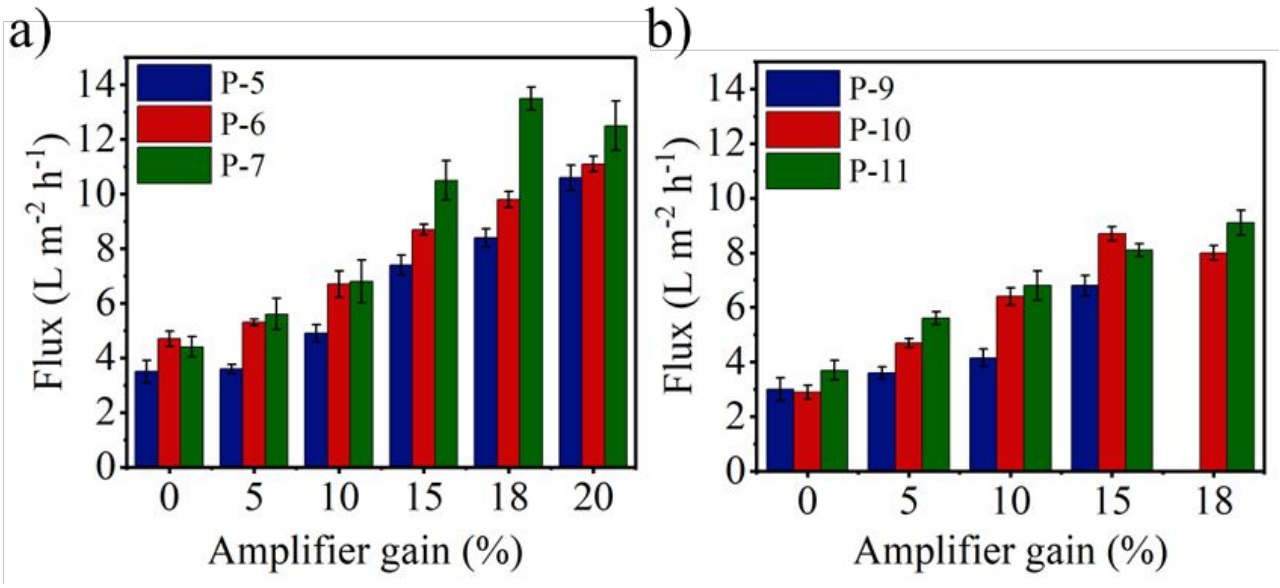

Figure 12: a) Membrane performance with RF heating for PES-LIG-18, and **b)** PES-LIG-22 membrane at 91 MHz.

In addition to RF parameters, and laser parameters, we studied VMD operating parameter, which also influence MD performance. The performance of MD with surface heating technique is highly influenced by MD operating parameters, such as the feed flow rate. In conventional MD, a higher flow rate (Reynolds number) is preferred in the feed channel to mitigate the TP effect, which is commonly achieved by introducing a spacer to increase the mixing within the feed channel. This higher velocity assists with 1) reducing the TP effect and 2) obtaining more suitable temperature profiles throughout the length of the MD module. Section S18 of Supporting Information elaborates on the effects of TP for conventional and surface-heated MD. Although helpful for the

MD cell to achieve a higher thermal efficiency, this higher flow rate leads to a significant energy inefficiency and loss at the system scale. Devising surface heating circumvents this shortcoming because the bulk feed temperature does not rapidly decline throughout the length of the membrane module, which is a major barrier to achieving reasonable energy efficiency and flux in large MD modules.[49] The bulk feed temperature actually increases slightly through the length of the surface-heated membrane configuration. Additionally, in the surface-heated membrane configuration, TP is not a major concern as the temperature driving force necessary for water evaporation is directly applied to the membrane surface, right at the place that mass transfer occurs. At any cross-section through the membrane module, the temperature of the water at the mass transfer interface remains higher than the bulk water temperature, but with adequate contact time (no slip condition), the feed water with the membrane will evaporate due to higher partial vapor pressure on the membrane feed side. This indicates that lower flow velocity would be more favorable for MD configuration with surface-heated membranes. To validate this, we studied the effect of feed flow rate in surface-heated VMD tests with PES-LIG-18 membrane at 91 MHz. Keeping RF input power constant (gain 0%), the feed flow rate was varied at 3.5, 5.0, 10.0, and 30.0 L/h. We used gain 0% to evaluate the sensitivity to the flow rate at the lowest power input. It was found that the increase in the feed flow rate led to a sharp decline in the MD flux, as displayed in Figure 13. This proves enhanced VMD performance can be achieved by lowering the flow rate for surface-heated desalination with VMD. Besides reduced flow rate, heat transfer efficiency can be enhanced by designing longer modules. This is important as it will lead to higher process-level efficiencies.

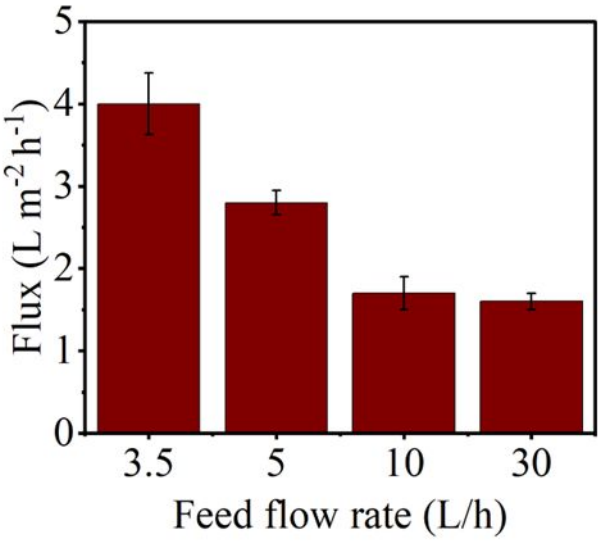

Figure 13: Effect of feed flow rate for PES-LIG-18 membrane in RF heated MD at 91 MHz and gain 0%.

Eventually, a VMD experiment was carried out with a PES-LIG-18 membrane for four days to investigate the feasibility and stability of the prepared membranes for long-term operation. The flux and permeate conductivity have been reported in Figure 14. Amplifier gain 0% was applied for the experiment, and the flux was found to be ~5 L m^{-2} h^{-1} with a slight decrease over the period of four days. The permeate conductivity was found to be consistently in the range of 2 – 10 µS, which proves the stable performance of our PES-LIG membrane under RF field.

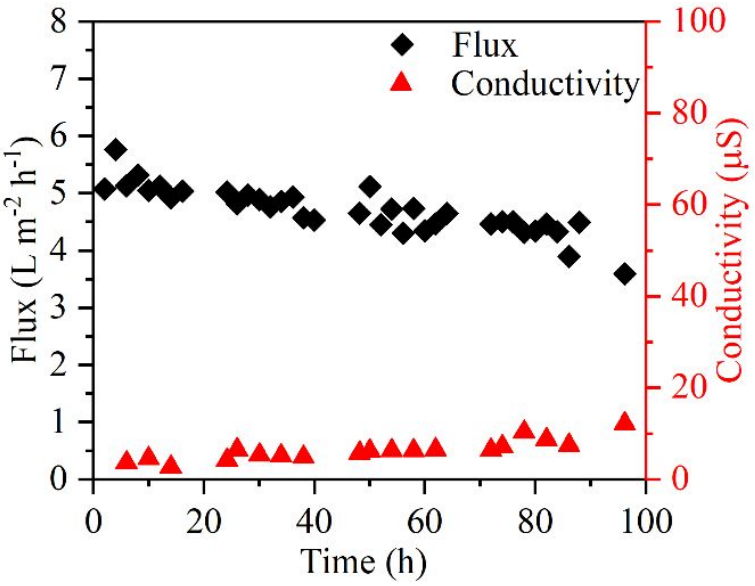

Figure 14: Long-term RF heated MD for 4 days with PES-LIG-18 membrane at 91 MHz and gain 0%.

Table 1 summarizes MD performance of recent literate with different electroconductive membranes and heating techniques compared to this study. RF surface-heated membranes for MD application has not been ever reported. As summarized in Table 1, RF-heated membrane displayed the second highest MD flux (second to a modified PVDF membrane). Thus, this work highlights the promise of RF for surface heating of MD membrane for the first time.

Table 1: Comparison of the best MD fluxes achieved with membrane surface heating from recent literature on surface-heated MD applications.

Membrane	Heating method	Flux ($L\ m^{-2}\ h^{-1}$)	Ref.
CNS-PP	Joule heating	~1.9	[50]
Carbon black - PVDF	Photothermal	1.71	[24]
Graphene – PVDF	Joule heating	23.44	[51]
Fe-CNT - PTFE	Induction heating	4.0	[52]
CNT-PVA - PTFE	Joule heating	7.5	[19]
$AgNO_3$ - PVDF	Photothermal	2.5	[53]
MWCNT - PVDF	Joule heating	2.77	[20]
MXene/PET - PTFE	Joule heating	1.8	[54]
MWCNT - PVDF	Coupled Joule and photothermal heating	1.1	[17]
LIG - PES	Joule heating	2.46	[28]
LIG-PES (Vector mode lasing)	**RF heating**	**13.5**	**This study**

3. Conclusion

We report a simple and scalable fabrication method to prepare advanced functional laser-ablated graphene membranes and investigated its performance for MD desalination. PES membrane substrate was prepared by phase inversion and soaked in $CaCl_2$ coagulation bath, which helped with protecting the membrane porous nanofeatures during fabrication and laser writing. Optimized laser parameters were identified for all the membranes made with different PES concentrations. Contact angle as high as ~144° was found in this work at the optimized laser settings. RF heating performance was also studied, and optimum RF frequency was identified with the reflection coefficient measurements. It was found that RF frequency of 91 MHz delivers the best

performance for our setup in terms of heating rate and VMD performance. VMD flux as high as ~13.5 $Lm^{-2}h^{-1}$ and 9.1 $Lm^{-2}h^{-1}$ were obtained for the PES-LIG-18, and PES-LIG-22 membranes in the RF field. Long-term VMD performance was tested for four days, resulting in stable flux and permeate conductivity, which suggests the robust performance of PES-LIG membranes for surface-heated MD application.

Experimental Section

Chemicals and Materials: Polyethersulfone (PES) powder (Veradel® 3000P) was obtained from Solvay Specialty Polymer, (Alorton, IL). 1-Methyl-2-pyrrolidinone (NMP) and sodium chloride (NaCl) was purchased from Fisher Scientific (Fair Lawn, NJ). Calcium chloride was purchased from VWR International (Radnor, PA). Deionized (DI) water (18.2 MΩ) was collected from Millipore Milli-Q water system (Billerica, MA).

Substrate Fabrication, Heating, and Characterization: PES membrane substrate was prepared via NIPS technique. Details on PES membrane substrate formation is provided in Section S1.1. CO_2 Laser treatment of the PES membrane substrate is also discussed in Section S1.2. Details on characterization of the substrate, LIG, and membranes are provided in Section S1.3. RF heating procedure is discussed in Section S1.4. VMD experimental setup is discussed in Section S1.5.

4. Supporting Information

Sections on Materials fabrication and characterization; Laser ablation; RF heating; VMD experimental setup; Mechanism of LIG formation; Contact angle; SEM analysis; Lasing surface selection; EDS mapping; XPS; Pore size distribution; TGA; FLIR response; Concept of surface heating; Effects of TP in MD.

5. Acknowledgments

The authors gratefully acknowledge financial support from The Bureau of Reclamation's Desalination and Water Purification Research Program (DWPR) under contract R22AC00435. The authors also acknowledge partial financial support from RAPID Manufacturing Institute - Advanced Manufacturing Office (AMO) under the award number DE-EE0007888-08-08. Sr.

Juliusz Warzywoda is acknowledged for assisting with characterizing LIG samples with X-ray photoelectron spectroscopy analysis. Fouzia H. Nowrin and Md. Shahriar Rahman are acknowledged for BET and TGA analysis respectively.

6. Conflict of Interest

The authors declare that they have no conflicts of interest.

7. References

[1] Mekonnen, M. M.; Hoekstra, A. Y. Four billion people facing severe water scarcity. *Science advances* **2016**, *2* (2), e1500323.
[2] Francis, L.; Ahmed, F. E.; Hilal, N. Advances in Membrane Distillation Module Configurations. *Membranes* **2022**, *12* (1), 81. DOI: 10.3390/membranes12010081.
[3] Alkhudhiri, A.; Hilal, N., *3 - Membrane distillation—Principles, applications, configurations, design, and implementation*, in *Emerging Technologies for Sustainable Desalination Handbook*, Gude, V. G., Editor. 2018, Butterworth-Heinemann. p. 55-106.
[4] Alkhudhiri, A.; Darwish, N.; Hilal, N. Membrane distillation: A comprehensive review. *Desalination* **2012**, *287*, 2-18. DOI: 10.1016/j.desal.2011.08.027.
[5] Schwantes, R.; Cipollina, A.; Gross, F.; Koschikowski, J.; Pfeifle, D.; Rolletschek, M.; Subiela, V. Membrane distillation: Solar and waste heat driven demonstration plants for desalination. *Desalination* **2013**, *323*, 93-106. DOI: 10.1016/j.desal.2013.04.011.
[6] Deshmukh, A.; Boo, C.; Karanikola, V.; Lin, S.; Straub, A. P.; Tong, T.; Warsinger, D. M.; Elimelech, M. Membrane distillation at the water-energy nexus: limits, opportunities, and challenges. *Energy & Environmental Science* **2018**, *11* (5), 1177-1196, 10.1039/C8EE00291F. DOI: 10.1039/C8EE00291F.
[7] Ravi, J.; Othman, M. H. D.; Matsuura, T.; Ro'Il Bilad, M.; El-Badawy, T. H.; Aziz, F.; Ismail, A. F.; Rahman, M. A.; Jaafar, J. Polymeric membranes for desalination using membrane distillation: A review. *Desalination* **2020**, *490*, 114530. DOI: 10.1016/j.desal.2020.114530.
[8] Wang, P.; Chung, T.-S. Recent advances in membrane distillation processes: Membrane development, configuration design and application exploring. *Journal of Membrane Science* **2015**, *474*, 39-56. DOI: 10.1016/j.memsci.2014.09.016.
[9] Tibi, F.; Charfi, A.; Cho, J.; Kim, J. Fabrication of polymeric membranes for membrane distillation process and application for wastewater treatment: Critical review. *Process Safety and Environmental Protection* **2020**, *141*, 190-201. DOI: 10.1016/j.psep.2020.05.026.
[10] Teoh, M. M.; Chung, T.-S. Membrane distillation with hydrophobic macrovoid-free PVDF–PTFE hollow fiber membranes. *Separation and Purification Technology* **2009**, *66* (2), 229-236. DOI: 10.1016/j.seppur.2009.01.005.
[11] Edwie, F.; Teoh, M. M.; Chung, T.-S. Effects of additives on dual-layer hydrophobic–hydrophilic PVDF hollow fiber membranes for membrane distillation and continuous performance. *Chemical Engineering Science* **2012**, *68* (1), 567-578. DOI: https://doi.org/10.1016/j.ces.2011.10.024.

[12] Fahmey, M. S.; El-Aassar, A.-H. M.; M.Abo-Elfadel, M.; Orabi, A. S.; Das, R. Comparative performance evaluations of nanomaterials mixed polysulfone: A scale-up approach through vacuum enhanced direct contact membrane distillation for water desalination. *Desalination* **2019**, *451*, 111-116. DOI: https://doi.org/10.1016/j.desal.2017.08.020.
[13] Kyoungjin An, A.; Lee, E.-J.; Guo, J.; Jeong, S.; Lee, J.-G.; Ghaffour, N. Enhanced vapor transport in membrane distillation via functionalized carbon nanotubes anchored into electrospun nanofibres. *Scientific Reports* **2017**, *7* (1), 41562. DOI: 10.1038/srep41562.
[14] Soukane, S.; Son, H. S.; Mustakeem, M.; Obaid, M.; Alpatova, A.; Qamar, A.; Jin, Y.; Ghaffour, N. Materials for energy conversion in membrane distillation localized heating: Review, analysis and future perspectives of a paradigm shift. *Renewable and Sustainable Energy Reviews* **2022**, *167*, 112702. DOI: https://doi.org/10.1016/j.rser.2022.112702.
[15] Kuang, Z.; Long, R.; Liu, Z.; Liu, W. Analysis of temperature and concentration polarizations for performance improvement in direct contact membrane distillation. *International Journal of Heat and Mass Transfer* **2019**, *145*, 118724. DOI: https://doi.org/10.1016/j.ijheatmasstransfer.2019.118724.
[16] Ahmed, F. E.; Lalia, B. S.; Hashaikeh, R.; Hilal, N. Alternative heating techniques in membrane distillation: A review. *Desalination* **2020**, *496*, 114713. DOI: https://doi.org/10.1016/j.desal.2020.114713.
[17] Huang, J.; Tang, T.; He, Y. Coupling photothermal and Joule-heating conversion for self-heating membrane distillation enhancement. *Applied Thermal Engineering* **2021**, *199*, 117557. DOI: https://doi.org/10.1016/j.applthermaleng.2021.117557.
[18] Arian, E.; Mohtada, S.; André, M. Fabrication of Joule heating coating layers by way of flame spraying for membrane distillation. *Surface Innovations* **2022**, *10* (4-5), 263-277. DOI: 10.1680/jsuin.21.00008.
[19] Dudchenko, A. V.; Chen, C.; Cardenas, A.; Rolf, J.; Jassby, D. Frequency-dependent stability of CNT Joule heaters in ionizable media and desalination processes. *Nature Nanotechnology* **2017**, *12* (6), 557-563. DOI: 10.1038/nnano.2017.102.
[20] Huang, J.; He, Y.; Shen, Z. Joule heating membrane distillation enhancement with multi-level thermal concentration and heat recovery. *Energy Conversion and Management* **2021**, *238*, 114111. DOI: https://doi.org/10.1016/j.enconman.2021.114111.
[21] Razaqpur, A. G.; Wang, Y.; Liao, X.; Liao, Y.; Wang, R. Progress of photothermal membrane distillation for decentralized desalination: A review. *Water Research* **2021**, *201*, 117299. DOI: https://doi.org/10.1016/j.watres.2021.117299.
[22] Qing, W.; Hu, Z.; Ma, Q.; Zhang, W. Conductive Fe3O4/PANI@PTFE membrane for high thermal efficiency in interfacial induction heating membrane distillation. *Nano Energy* **2021**, *89*, 106339. DOI: https://doi.org/10.1016/j.nanoen.2021.106339.
[23] Politano, A.; Argurio, P.; Di Profio, G.; Sanna, V.; Cupolillo, A.; Chakraborty, S.; Arafat, H. A.; Curcio, E. Photothermal Membrane Distillation for Seawater Desalination. *Advanced Materials* **2017**, *29* (2), 1603504. DOI: https://doi.org/10.1002/adma.201603504.
[24] Wu, J.; Zodrow, K. R.; Szemraj, P. B.; Li, Q. Photothermal nanocomposite membranes for direct solar membrane distillation. *Journal of Materials Chemistry A* **2017**, *5* (45), 23712-23719, 10.1039/C7TA04555G. DOI: 10.1039/C7TA04555G.
[25] Wu, X.; Cao, S.; Ghim, D.; Jiang, Q.; Singamaneni, S.; Jun, Y.-S. A thermally engineered polydopamine and bacterial nanocellulose bilayer membrane for photothermal membrane distillation with bactericidal capability. *Nano Energy* **2021**, *79*, 105353. DOI: https://doi.org/10.1016/j.nanoen.2020.105353.

[26] Gao, M.; Peh, C. K.; Meng, F. L.; Ho, G. W. Photothermal Membrane Distillation toward Solar Water Production. *Small Methods* **2021**, *5* (5), 2001200. DOI: https://doi.org/10.1002/smtd.202001200.
[27] Lotfy, H. R.; Staš, J.; Roubík, H. Renewable energy powered membrane desalination—review of recent development. *Environmental Science and Pollution Research* **2022**, *29* (31), 46552-46568.
[28] Tan, Y. Z.; Kapavarapu, M. S. R. S.; Oor, J. Z.; Ong, C. S.; Chew, J. W. Laser-induced graphene Janus membrane for electrothermal membrane distillation. *Desalination* **2022**, *540*, 115994. DOI: https://doi.org/10.1016/j.desal.2022.115994.
[29] Vashisth, A.; Upama, S. T.; Anas, M.; Oh, J.-H.; Patil, N.; Green, M. J. Radio frequency heating and material processing using carbon susceptors. *Nanoscale Advances* **2021**, *3* (18), 5255-5264, 10.1039/D1NA00217A. DOI: 10.1039/D1NA00217A.
[30] Khan, W. S.; Asmatulu, R.; Ceylan, M.; Jabbarnia, A. Recent progress on conventional and non-conventional electrospinning processes. *Fibers and Polymers* **2013**, *14* (8), 1235-1247. DOI: 10.1007/s12221-013-1235-8.
[31] Dong, X.; Lu, D.; Harris, T. A.; Escobar, I. C. Polymers and solvents used in membrane fabrication: a review focusing on sustainable membrane development. *Membranes* **2021**, *11* (5), 309.
[32] Szabó, A.; Perri, C.; Csató, A.; Giordano, G.; Vuono, D.; Nagy, J. B. Synthesis Methods of Carbon Nanotubes and Related Materials. *Materials* **2010**, *3* (5), 3092-3140. DOI: 10.3390/ma3053092.
[33] Sianipar, M.; Kim, S. H.; Khoiruddin; Iskandar, F.; Wenten, I. G. Functionalized carbon nanotube (CNT) membrane: progress and challenges. *RSC Advances* **2017**, *7* (81), 51175-51198, 10.1039/C7RA08570B. DOI: 10.1039/C7RA08570B.
[34] Thakur, A. K.; Mahbub, H.; Nowrin, F. H.; Malmali, M. Highly Robust Laser-Induced Graphene (LIG) Ultrafiltration Membrane with a Stable Microporous Structure. *ACS Applied Materials & Interfaces* **2022**, *14* (41), 46884-46895. DOI: 10.1021/acsami.2c09563.
[35] Bayati, M.; Peng, H.; Deng, H.; Lin, J.; Fidalgo de Cortalezzi, M. Laser induced graphene /ceramic membrane composite: Preparation and characterization. *Journal of Membrane Science* **2020**, *595*, 117537. DOI: https://doi.org/10.1016/j.memsci.2019.117537.
[36] Ye, R.; James, D. K.; Tour, J. M. Laser-induced graphene. *Accounts of chemical research* **2018**, *51* (7), 1609-1620.
[37] Mahbub, H.; Saed, M. A.; Malmali, M. Pattern-Dependent Radio Frequency Heating of Laser-Induced Graphene Flexible Heaters. *ACS Applied Materials & Interfaces* **2023**, *15* (14), 18074-18086. DOI: 10.1021/acsami.3c00569.
[38] Nasser, J.; Lin, J.; Zhang, L.; Sodano, H. A. Laser induced graphene printing of spatially controlled super-hydrophobic/hydrophilic surfaces. *Carbon* **2020**, *162*, 570-578.
[39] Tittle, C. M.; Yilman, D.; Pope, M. A.; Backhouse, C. J. Robust superhydrophobic laser-induced graphene for desalination applications. *Advanced Materials Technologies* **2018**, *3* (2), 1700207.
[40] Guo, Y.; Zhang, C.; Chen, Y.; Nie, Z. Research Progress on the Preparation and Applications of Laser-Induced Graphene Technology. *Nanomaterials* **2022**, *12* (14), 2336. DOI: 10.3390/nano12142336.
[41] Lin, J.; Peng, Z.; Liu, Y.; Ruiz-Zepeda, F.; Ye, R.; Samuel, E. L. G.; Yacaman, M. J.; Yakobson, B. I.; Tour, J. M. Laser-induced porous graphene films from commercial polymers. *Nature Communications* **2014**, *5* (1), 5714. DOI: 10.1038/ncomms6714.

[42] Bergsman, D. S.; Getachew, B. A.; Cooper, C. B.; Grossman, J. C. Preserving nanoscale features in polymers during laser induced graphene formation using sequential infiltration synthesis. *Nature Communications* **2020**, *11* (1), 3636. DOI: 10.1038/s41467-020-17259-5.
[43] Li, Y.; Luong, D. X.; Zhang, J.; Tarkunde, Y. R.; Kittrell, C.; Sargunaraj, F.; Ji, Y.; Arnusch, C. J.; Tour, J. M. Laser-Induced Graphene in Controlled Atmospheres: From Superhydrophilic to Superhydrophobic Surfaces. *Advanced Materials* **2017**, *29* (27), 1700496. DOI: 10.1002/adma.201700496.
[44] Wu, W.; Liang, R.; Lu, L.; Wang, W.; Ran, X.; Yue, D. Preparation of superhydrophobic laser-induced graphene using taro leaf structure as templates. *Surface and Coatings Technology* **2020**, *393*, 125744. DOI: 10.1016/j.surfcoat.2020.125744.
[45] Rekhi, S.; Tempere, J.; Silvera, I. F. Temperature determination for nanosecond pulsed laser heating. *Review of Scientific Instruments* **2003**, *74* (8), 3820-3825. DOI: 10.1063/1.1593790.
[46] He, T.; Blume, I. A process for drying a wet porous membrane structure and the porous membrane structure obtained from said process. *European Patent EP1466659 A* **2003**, *1*, 2004.
[47] Cao, L.; Zhu, S.; Pan, B.; Dai, X.; Zhao, W.; Liu, Y.; Xie, W.; Kuang, Y.; Liu, X. Stable and durable laser-induced graphene patterns embedded in polymer substrates. *Carbon* **2020**, *163*, 85-94. DOI: https://doi.org/10.1016/j.carbon.2020.03.015.
[48] Peng, Z.; Lin, J.; Ye, R.; Samuel, E. L. G.; Tour, J. M. Flexible and Stackable Laser-Induced Graphene Supercapacitors. *ACS Applied Materials & Interfaces* **2015**, *7* (5), 3414-3419. DOI: 10.1021/am509065d.
[49] Islam, M. R.; Lin, B.; Yu, Y.; Chen, C.-C.; Malmali, M. Comparative Energetics of Various Membrane Distillation Configurations and Guidelines for Design and Operation. *Membranes* **2023**, *13* (3), 273.
[50] Ahmed, F. E.; Lalia, B. S.; Hashaikeh, R.; Hilal, N. Intermittent direct joule heating of membrane surface for seawater desalination by air gap membrane distillation. *Journal of Membrane Science* **2022**, *648*, 120390. DOI: https://doi.org/10.1016/j.memsci.2022.120390.
[51] T. M, S.; Lin, P. T.; Chiao, Y.-H.; Widakdo, J.; Chuang, C.-H.; Rahmadhanty, S. F.; Yoshikawa, S.; Hung, W.-S. High performance self-heated membrane distillation system for energy efficient desalination process. *Journal of Materials Chemistry A* **2021**, *9* (12), 7868-7880, 10.1039/D0TA11724B. DOI: 10.1039/D0TA11724B.
[52] Anvari, A.; Kekre, K. M.; Azimi Yancheshme, A.; Yao, Y.; Ronen, A. Membrane distillation of high salinity water by induction heated thermally conducting membranes. *Journal of Membrane Science* **2019**, *589*, 117253. DOI: https://doi.org/10.1016/j.memsci.2019.117253.
[53] Ye, H.; Li, X.; Deng, L.; Li, P.; Zhang, T.; Wang, X.; Hsiao, B. S. Silver Nanoparticle-Enabled Photothermal Nanofibrous Membrane for Light-Driven Membrane Distillation. *Industrial & Engineering Chemistry Research* **2019**, *58* (8), 3269-3281. DOI: 10.1021/acs.iecr.8b04708.
[54] Wang, Z.; Li, Z.; Yong, B.; Huang, H.; Yao, L.; Deng, L. Depression of electro-oxidation of Ti3C2Tx MXene Joule heater by alternating current for Joule heating membrane distillation. *Chemical Engineering Journal* **2023**, *461*, 142149. DOI: https://doi.org/10.1016/j.cej.2023.142149.

Data Availability Statement

The data supporting this article have been included as part of the Supplementary Information. Raw experimental data will become available upon request.